Title: In cell NMR reveals cells selectively amplify and structurally remodel amyloid fibrils

Authors: Shoyab Ansari[1]†, Dominique Lagasca[1]†, Rania Dumarieh[1], Yiling Xiao[1], Sakshi Krishna[1], Yang Li[1] & Kendra K. Frederick[1,2]*.

† These authors contributed equally.

Affiliations:

1. Department of Biophysics, UT Southwestern Medical Center, Dallas, TX 75390-8816.
2. Center for Alzheimer's and Neurodegenerative Disease, UT Southwestern Medical Center, Dallas, TX 75390

*To whom correspondance should be addressed: Kendra K. Frederick

Email: kendra.frederick@utsouthwestern.edu

http://orcid.org/0009-0009-0446-528X

https://orcid.org/0000-0003-4404-4366

https://orcid.org/0000-0002-4462-7134

https://orcid.org/0000-0002-4548-4833

https://orcid.org/0000-0002-4223-0379

https://orcid.org/0000-0001-9601-4885

https://orcid.org/0000-0002-1656-5167

Abstract:

Amyloid forms of α-synuclein adopt different conformations depending on environmental conditions. Advances in structural biology have accelerated fibril characterization. However, it remains unclear which conformations predominate in biological settings because current

methods typically not only require isolating fibrils from their native environments, but they also do not provide insight about flexible regions. To address this, we characterized α-syn amyloid seeds and used sensitivity enhanced nuclear magnetic resonance to investigate the amyloid fibrils resulting from seeded amyloid propagation in different settings. We found that the amyloid fold and conformational preferences of flexible regions are faithfully propagated *in vitro* and in cellular lysates. However, seeded propagation of amyloids inside cells led to the minority conformation in the seeding population becoming predominant and more ordered, and altered the conformational preferences of flexible regions. The examination of the entire ensemble of protein conformations in biological settings that is made possible with this approach may advance our understanding of protein misfolding disorders and facilitate structure-based drug design efforts.

Introduction:

Neurodegeneration in patients with Parkinson's disease is correlated with the occurrence of Lewy bodies—intracellular inclusions that contain fibrillar aggregates of the protein α-synuclein (α-syn). While α-syn is an intrinsically disordered monomer in solution, this 140 amino acid protein can and does spontaneously assemble into a variety of different self-templating fibrillar forms that differ by the number and location of β-sheets (*1*, *2*). The conformations that α-syn adopts are highly dependent upon differences in the environment and understanding which conformations are adopted in health and disease is critical to advancing our ability to rationally intervene. Advances in structural biology have enabled a rapid acceleration in the characterization of structures of amyloid fibrils (*2*, *3*). This wealth of structural data

promises to open the door for structure-informed development of tools for diagnostic, treatment response, and therapeutic development purposes. However, actualization of this promise requires knowledge of which structures are adopted in biological settings as well as their prevalence (*4*).

Determining which structures are adopted in biological settings is complicated because the adopted amyloid conformations depend upon the environment, but amyloid fibrils are isolated from their native environments for high resolution structural studies. Thus, the degree to which these structural models represent the conformations adopted in biological settings can often only be inferred. Experiments to connect structures of isolated amyloid fibrils to the structures in biological settings often take advantage of at least one of the unique biophysical properties of amyloid fibrils, such as the ability of small amounts of amyloid fibrils to template or "seed" the polymerization of monomeric protein into the amyloid form (*5*), or the higher thermodynamic stability and molecular weight of many amyloid fibrils relative to most other biomolecules(*6*). For example, the biological consequences of spontaneously formed fibrils *in vitro* can be assessed by introduction of these fibrils into biological settings. Such fibrils are often found to be competent to induce amyloid formation and/or toxicity in cellular systems that model aspects of neurodegenerative disease and/or induce neuropathology in murine disease models (*7-10*). However, if the resulting morphology of the α-syn fibril-induced aggregates in these settings is assessed, it is by low-resolution methods like immunohistochemistry or proteinase K digestion (*7-10*). Thus, the population of amyloid structures propagated in biological settings may not be the same as that of the seeding population (*9*). Conversely, amyloid fibrils can be extracted from the post-mortem tissues of individuals afflicted with α-synucleinopathies based upon their high molecular weight and stability in the presence of

detergents like sarkosyl (*11*). Interestingly, such *ex vivo* samples are typically mixtures of different amyloid forms and have relatively larger amyloid fibril cores which are flanked by "islands of density" that are attributed to partial occupancy by a flexible part of the protein (*1*, *12*, *13*). While variations in the stoichiometry and heterogeneity in the mixtures of amyloid forms across *ex vivo* samples and large amyloid cores may be a general feature of pathological amyloids, they could also result from variability in extraction efficiency across tissues and cryo-EM sample preparation (*14*), selection bias for thermodynamically-stable minority species, and conformational alterations from the extraction process (*15*). Thus, the structures derived from *ex vivo* material may not be those that are most prevalent in biological settings. Knowledge of which amyloid conformations are present as well as their relative abundance when propagated in both *in vitro* and cellular settings will address a current gap in our understanding of amyloid propagation and identify structural models that capture features of the dominant amyloid forms in biological settings of interest.

The gap in our understanding of amyloid structure and propagation is not limited to the conformations of the amyloid core. Indeed, the amyloid core sequesters only half of the residues of α-syn. The other half of the residues flank the amyloid core and are typically not visualizable by diffraction-based methods. Yet these flexible regions mediate both primary and secondary nucleation (*16-18*) as well as interactions of amyloid fibers with cellular constituents such as chaperone proteins (*19-23*). The flanking regions have important roles in aggregation, toxicity and cellular (dys)function (*24*, *25*), but structural information about them is lacking, both in purified as well as in biological settings. Knowledge of the conformational preferences of conformationally disordered regions could provide new opportunities to target disease-related aggregation.

Magic angle spinning (MAS) NMR of frozen solids can report on the identity and relative abundance of small variations in structure as well as on the ensemble of conformations sampled by regions of intrinsic disorder. The NMR line shapes of frozen protein samples are quantitative constraints on backbone conformational distributions (*26-29*). Moreover, while most structural biology approaches require purified samples, NMR spectroscopy does not, making it well-suited to study protein conformations of both ordered and disordered regions in native contexts. While solid state NMR is often limited by experimental sensitivity, the sensitivity of solid state NMR can be dramatically increased via dynamic nuclear polarization (DNP). For biological systems, these sensitivity gains are sufficient to enable specific detection of isotopically enriched proteins at concentrations and in environments that accurately model their native environments (*30-36*). Our group established sample handling methods for DNP MAS NMR that support data collection with high sensitivity gains on frozen cellular samples that remain intact and viable throughout the experiment (*34, 37-39*). Thus, DNP-assisted MAS NMR can quantitatively report on the entire conformational ensemble of a protein both *in vitro* as well as inside intact viable cells. Here, we use this method to directly determine if *in vitro* propagated amyloid conformations are faithfully propagated in cellular settings.

In this work, we use α-syn fibrils to seed α-syn polymerization *in vitro,* in concentrated cellular lysates, and directly inside living cells. To polymerize α-syn inside cells from an amyloid seed, we use a biosensor cell line designed to evaluate amyloid seeding (*40*). These HEK293T cells express α-syn harboring the pathogenic A53T mutation fused to either CFP or YFP. The α-syn(A53T)-CFP/YFP, which is constitutively amino-terminally acetylated in mammalian cells (*41*), remains soluble until the cells are exposed to α-syn fibril seeds (*41-44*). To eliminate any sequence-based structural incompatibility between the α-syn fibrils and the α-

syn inside the cells (*45*), we use *in vitro* formed fibrils of acetylated full-length α-syn(A53T) (Ac-α-syn(A53T)) as seeds (*46, 47*). We report the seeding efficiency and cytotoxicity associated with α-syn aggregation in these biosensor cells. We then determine structural features of the amyloid core and the intrinsically disordered flanking regions of Ac-α-syn(A53T) fibril seeds as well as fibrils propagated *in vitro*, in lysates and *in situ* inside biosensor cells using a combination of NMR spectroscopy and cryo-EM. Collectively, these experiments report on which amyloid conformations are present as well as their relative abundance when they are propagated *in vitro*, in cellular lysates, and inside cells.

Results

Ac-α-Syn(A53T) fibrils are polymorphic

To assess the conformation of α-syn fibrils by MAS NMR spectroscopy, we used valine chemical shifts as reporters of Ac-α-syn(A53T) amyloid fibril conformation. Following a published protocol (*46*), we formed *de novo* amyloid fibrils using purified amino terminally acetylated α-syn harboring the A53T mutation that was isotopically enriched with ^{13}C at all of the valines and ^{15}N at the single histidine (H50) in the α-syn sequence. As previously reported, the resulting fibrils had a single morphology with helical twist periodicity of 95 ± 2 nm by negative stain transmission electron microscopy (**Figure S1**).

To assess the conformational homogeneity at a single site in the amyloid fibril, we collected 2D NCOCx spectra at 104 K (*48*) (**Figure 1B**). This experiment is selective for V49. The chemical shifts of V49 are consistent with β-sheet conformations (*49*) and revealed a polymorphism at V49Cβ with a population of the major conformation of 79% and of the minor conformation of 21% (**Figure 1B**; **Table S1**). Predictions of the φ/ψ backbone torsion angles of

V49 from chemical shift and homology (*50*) indicated that the conformational change was small; the predicted dihedral angles at V49 were -132°/138° ± 20° for the major polymorph and -113°/136° ± 20° for the minor polymorph, a change that displaces the adjacent residues by less than 1 Å (**Figure 2C**). The major peak (V49Cβ) had a full width at half maximum (FWHM) of 2.0 ppm and the minor peak (V49Cβ') had a FWHM of 3.1 ppm (**Table S1**), which is ~0.5 ppm broader than the expected homogenous line width under these experimental conditions. The broader line indicates that the minor conformation samples a wider range of related conformations than the major conformation (*26-29*). Thus, examination of a single site by solid state NMR of a frozen sample enabled precise quantification of a small local structural polymorphism with atomic-level precision.

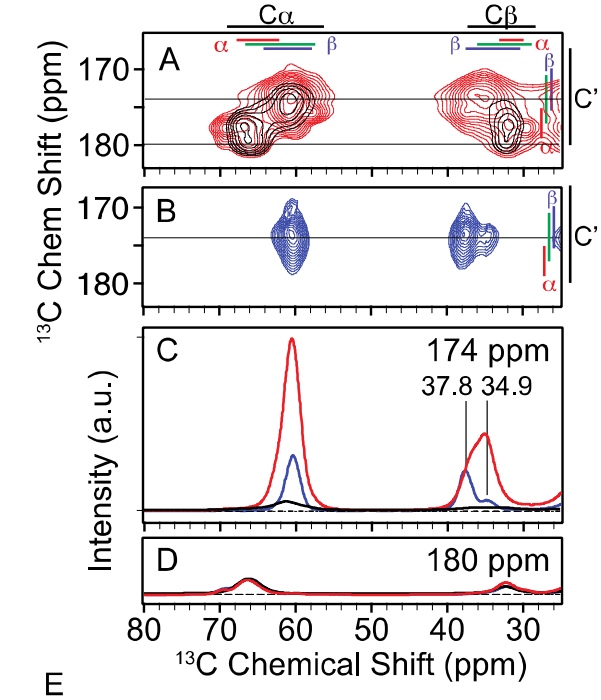

Figure 1*: A) Overlay of 2D ^{13}C–^{13}C DARR spectra of uniformly ^{13}C-valine labeled* Ac-α-syn(A53T) fibrils *(red) and segmentally ^{13}C-valine labeled fibrils where only the four N terminal valines (black) are labeled. Average chemical shifts +/- two standard deviation are marked for each atom (black) as well as for the α-helical (red), random coil (green), and β (blue) secondary structural elements. B) NCOCx spectra of uniformly ^{13}C-valine and ^{15}N-histidine labeled fibrils that is specific for V49 (blue). One-dimensional slice from the 2D spectra at C) 174 ppm and D) 180 ppm. The intensity of the V49 spectrum (blue) is displayed at 10 times the relative intensity for visibility and the peak centers are indicated. NMR spectra were recorded at a field strength of 14 T (600 MHz) and MAS frequencies of 12 kHz at 104 K. NMR samples were cryoprotected with 15% d_8-^{12}C-glycerol and doped with 7 mM AMUPol. E) Primary sequence of Ac-α-syn(A53T). The 19 valines (highlighted in red) are distributed throughout the sequence, with V49 bolded for emphasis. H50 is colored blue. Regions visible in the cryo-EM density for polymorph A (blue) and polymorph B (green) are underlined. The ligation site for segmental isotopic labeling is indicated by a triangle.*

To determine if the polymorphism was limited to V49 or represented a larger scale structural difference, we collected single particle cryo-EM data of the Ac-α-syn(A53T) amyloid fibrils. Two polymorphs were distinguished in the 2D class averages and the reconstructed cryo-EM 3D density maps had overall resolutions of 2.2 Å for polymorph A and 2.7 Å for polymorph B (**Figure 2, Figure S2, Table S2**). The polymorphism observed by NMR was not limited to V49; these two polymorphs differed in the dihedral angles at V49 — the φ/ψ backbone torsion angles for V49 in polymorph A were -131°/134° and in polymorph B were -106°/136° (**Figure 2C**) — as well as in the number of residues sequestered in the amyloid core (14-22 & 36-92 *vs.* 36-92), the main chain traces (e.g. at residues 63-70 and 83-92) and, most strikingly, the protofilament interfaces (**Figure 2D**). While fibrils of both polymorphs consisted of two protofilaments with a Greek-key like architecture (r.m.s.d. = 0.8 Å for 68% of the residues), the protofilament interface of polymorph A involved only K45 and E46 and buried ~139 $Å^2$ of

solvent accessible surface area per monomer and the protofilament interface of polymorph B spanned residues 45-55 and buried ~316 $Å^2$ of solvent accessible surface area per monomer. Thus, the polymorphism we observed at V49 was not limited to a single site; the two polymorphs differed in the details of the protofilament fold and the ultra-structural morphology of the protofilament interfaces. Therefore, changes at V49 report on both local and large-scale rearrangements of fibril conformations, including large changes in the buried and exposed surfaces of the fibrils.

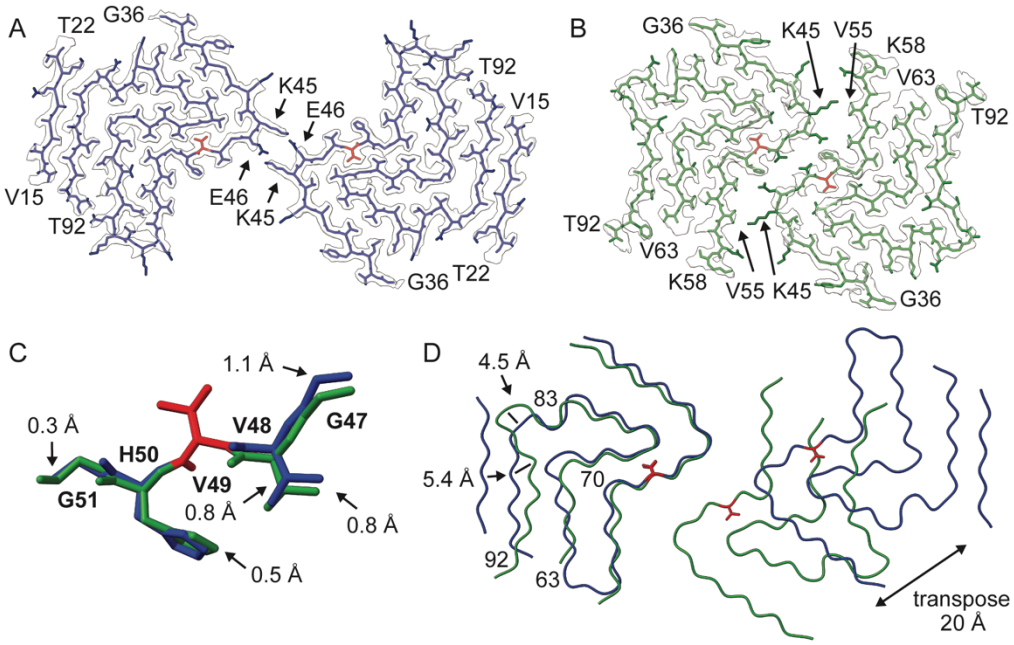

Figure 2: The cryo-EM analysis of Ac-α-syn(A53T) fibrils reveals two distinct polymorphs. *One layer of the fibril structure model in the cryo-EM reconstruction density map of A) polymorph A (blue) and B) polymorph B (green) with V49 highlighted in red and the starting and ending residues of protofilaments interfaces are annotated with arrows. C) local structural variation (G47 to G51) between polymorph A and B when V49 (red) is fixed. D) Overlay of a single layer of polymorph A (blue) and B (green) based on the alignment of the Cα atoms of one protofilament subunit highlight small changes in the protofilament fold between residues 63-70 and 83-92 as well as 20 Å*

The site-specific quantitative information about the structural ensemble from NMR can be linked to the cryo-EM structures through the relationship of NMR chemical shift to dihedral angles as well as the measurements of relative molecular order reported by NMR peak widths and cryo-EM resolution. The predicted dihedral angles from chemical shifts for the major polymorph agree with those for the cryo-EM structure of polymorph A and those for the minor polymorph agree with those for the structure of polymorph B. Moreover, the narrower NMR peak width for the major polymorph indicates higher molecular order, in line with better molecular alignment that resulted in a higher resolution map for polymorph A, while the broader NMR peak width for the minor polymorph indicates lower molecular order, in line with the poorer molecular alignment and lower resolution map for polymorph B (**Figure 2, Table S2**). Thus, polymorph A represents the major conformation observed by NMR spectroscopy for *de novo* Ac-α-syn(A53T) fibrils *in vitro* while polymorph B represents the minor conformation. The NMR spectra of the frozen fibril sample provide site-specific quantitative ensemble-based information that informs on the population of the polymorphs in the sample.

Flanking disordered regions of amyloid fibrils have conformational preferences *in vitro*

Of the 19 valines in α-syn, three-quarters of the valine residues are in the β-sheet and turn rich amyloid core and a quarter of the valine residues are in the disordered flanking regions that are not resolvable by cryo-EM (*46*). To assess the conformation of the valines in our amyloid fibrils, we collected a 2D ^{13}C–^{13}C dipolar assisted rotational resonance (DARR) correlation spectrum at 104 K. The majority of the cross peak intensity (82% ± 3%) had chemical shifts consistent with β-strand and random coil secondary structure backbone conformations(*49*) **(Figure 1,** red). However, a minority of the cross peak intensity (18% ± 3%) had chemical shifts

consistent with α-helical backbone conformations (*49*). Because the valines in the amyloid core are in β-strands and turns, these data suggested that the valine residues in the amino terminal region may adopt dihedral angles that can result in α-helical conformations.

To determine if the flanking disordered region of Ac-α-syn(A53T) fibrils had strong preferences to adopt dihedral angles that can result in α-helical conformations, we formed amyloid fibrils from Ac-α-syn(A53T) that was isotopically enriched with ^{13}C at only the four valines in the amino terminal region and collected a 2D ^{13}C-^{13}C DARR spectrum at 104 K (**Figure 1,** black). We found that the majority of the cross-peak intensity for the four valines in the amino terminus (V3, V15, V16, and V26) had chemical shifts consistent with α-helical backbone conformations (67% ± 8%) and a minority of the cross-peak intensity had chemical shifts consistent with β-strands and random coil backbone conformations (32% ± 8%) (**Figure 1C, 1D**). These peaks could not be definitively assigned to specific residues. However, based upon the cryo-EM densities and the relative populations of the different fibril polymorphs, the cross peak with chemical shifts consistent with α-helical backbone conformations was attributed to V3 and V26 in both fibril polymorphs and V15 & V16 in the polymorph B fibril form and the cross peak with chemical shifts consistent with β-strands and coil backbone conformations was attributed to V15 and V16 in the polymorph A fibril form. Most of the amino terminal region (residues 1-36) was not observable in the cryo-EM structure of either polymorph, indicating significant conformational heterogeneity for this region. However, in polymorph A, an eight amino acid long segment (V15-T22) of the amino terminus adopted a β-strand that encompassed two of the four isotopically labeled valine residues (V15 & V16) (**Figure 2A**). The φ torsion angle for V15 was undefined because conformational heterogeneity resulted in insufficient cryo-EM density to place the preceding G14 residue and the ψ backbone torsion angle for V15 was

109°, therefore V15 likely adopts a family of β-strand and/or coil conformations. The φ/ψ backbone torsion angles for V16 in polymorph A were -135°/137°, therefore V16 adopted a β-strand conformation in this fibril form. Because V15 and V16 in polymorph A each account for ~20% of the total peak intensity for the ensemble of segmentally isotopically labeled Ac-α-syn(A53T) fibrils, together V15 and V16 in polymorph A accounted for the entirety of the intensity of the cross peak with chemical shifts consistent with β-strands and coil backbone conformations. Thus, at 104 K, NMR analysis indicates that the valines in the amino terminal region that were not visualizable by cryo-EM had conformational preferences and that those disordered regions preferentially sampled the dihedral angles that can result in α-helical conformations. Finally, comparison of the spectra of the segmentally isotopically labeled Ac-α-syn(A53T) fibrils to the spectra of uniformly ^{13}C valine labeled Ac-α-syn(A53T) fibrils revealed that the majority (~80%) of the cross-peak intensity in the α-helical region of the 2D DARR spectrum of uniformly ^{13}C valine labeled Ac-α-syn(A53T) fibrils was accounted for by the four amino terminal valine residues (**Figure 1**). Therefore, the peaks in the α-helical region of *de novo* fibrils *in vitro* report on the valines in the amino terminal disordered flanking region. Collectively, investigation of *de novo* Ac-α-syn(A53T) fibrils *in vitro* by DNP NMR revealed both conformational preferences for the amino terminal disordered region that flanks the amyloid core as well as quantification of polymorphism in the amyloid core of these fibrils that could be linked to solved cryo-EM structures.

Ac-α-syn-(A53T) fibrils seed true *in vitro*

To determine if the conformation of *de novo* Ac-α-syn(A53T) fibrils could be faithfully propagated *in vitro*, we added a small amount (1% monomer/monomer) of pre-formed *de novo*

Ac-α-syn(A53T) fibrils to seed amyloid propagation in a solution of monomeric isotopically labeled Ac-α-syn(A53T). The monomeric Ac-α-syn(A53T) was allowed to polymerize. Both the 1D NCoCx and 2D ^{13}C-^{13}C DARR spectra of the resulting fibrils were indistinguishable from those of the *de novo* formed Ac-α-syn(A53T) fibrils (**Figure S3, Table S4**), indicating that both the conformations and populations of the two polymorphs and the conformational preferences of the amino terminal disordered domain of these fibrils were faithfully propagated *in vitro*.

Seeded amplification of isotopically labeled Ac-α-syn-(A53T) fibrils in cells is efficient and cytotoxic

To determine if the conformation of Ac-α-syn(A53T) fibrils could be faithfully propagated inside cells, we used Ac-α-syn(A53T) fibrils to seed amyloid formation in a biosensor cell line that was developed to propagate α-syn amyloid conformations in response to exposure to α-syn amyloid seeds (*40*). We first assessed the seeding efficiency of Ac-α-syn(A53T) fibrils in this cell line. These HEK293T cells stably express soluble α-syn(A53T) fused via an 18 amino acid long linker to either CFP or YFP (*41-44*), a modification that does not alter seeding efficiency (*47*). When α-syn(A53T) aggregates, the attached CFP and YFP are brought into proximity and act as a FRET pair so the formation of aggregates can be quickly and easily visualized and quantitated by fluorescence microscopy and flow cytometry. Seeding of the α-syn(A53T) biosensor cells with Ac-α-syn(A53T) amyloid fibrils was efficient; 71.1% ± 0.4% of cells were FRET-positive post exposure to Ac-α-syn(A53T) fibril seeds (**Figure 3A & 3B**).

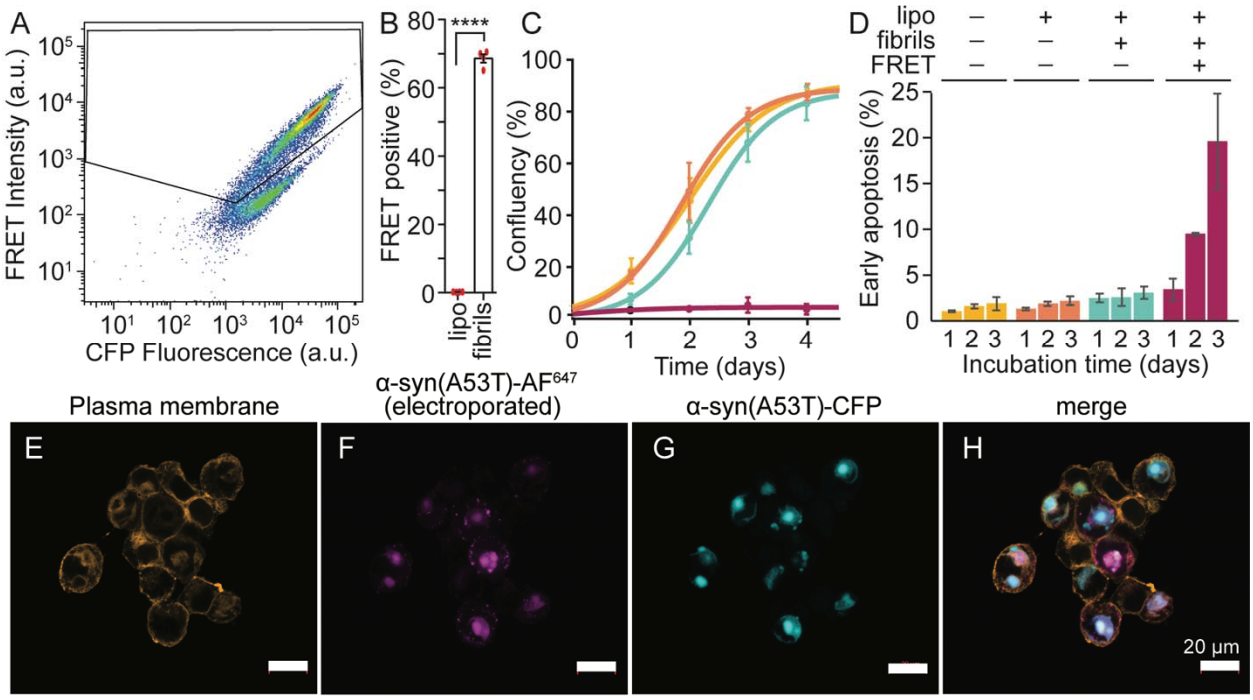

Figure 3: Ac-α-syn(A53T) seeding of *α-syn sensor cell lines is efficient and aggregation is cytotoxic. A) Flow cytometry reports on seeding efficiency of Ac-α-syn(A53T) preformed fibrils for the α-syn(A53T)-CFP/YFP HEK293T biosensor cell line after 24 hours incubation. B) Quantification of cytometry experiments, p = 0.0001, paired t-test of fibril-treated versus lipofectamine treated cells. Error bars are ± S.E.M; n=4. C) Cells harboring aggregates do not propagate. Cultured FRET-negative cells after exposure to buffer (yellow), lipofectamine (orange), or lipofectamine and fibrils (blue) grew to confluency after 4 days while FRET-positive cells exposed to lipofectamine and fibrils (pink) did not. Data are average ± standard deviation; n=3. D) The population of cells in early apoptosis as assessed by Annexin V and PI staining increases with increasing incubation time. Data are average ± standard deviation; n=4. E-H) Colocalization of electroporated Alexa 647–tagged Ac-α-syn(A53T) with Ac-α-syn(A53T)-CFP in biosensor cells after seeding. Exogenously produced Ac-α-syn(A53T) labeled with Alexa fluor 647 (AF^{647}) was electroporated into the biosensor cells (pink) and, upon exposure to Ac-α-syn(A53T) fibrils, colocalized with the endogenously expressed Ac-α-syn(A53T)-CFP aggregates (cyan) (Pearson's coefficient = 0.62).*

To determine if the cellular aggregates that formed in response to seeding by Ac-α-syn(A53T) fibrils were cytotoxic, we sorted the biosensor cells seeded with Ac-α-syn(A53T) fibrils and determined the growth kinetics of the FRET-negative and FRET-positive cell populations. We found that FRET-negative cells grew to confluency after 4 days while the FRET-positive cells did not grow in that time (**Figure 3C**). Thus, the presence of aggregated α-syn(A53T)-CFP/YFP inside cells stopped cell growth. To determine if the presence of aggregates was cytotoxic to cells, we quantitated apoptotic cell death in FRET-negative and FRET-positive cells using flow cytometry analysis of annexin V and propidium iodide stained cells (*51*). We found that 2.4% ± 0.5% of FRET-negative cells were in early apoptosis 24 hours after exposure to fibrils and this proportion didn't change with increasing incubation times. In contrast, 3.4% ± 1.2% of the FRET-positive cells were apoptotic 24 hours after exposure to fibrils and this proportion increased with increasing incubation time to 19% ± 5% after three days (**Figure 3D**). Thus, Ac-α-syn(A53T) fibril-induced aggregation in α-syn(A53T) biosensor cells is efficient and the presence of the aggregates is cytotoxic.

To determine if exogenously produced Ac-α-syn(A53T) behaved like the Ac-α-syn(A53T)-CFP/YFP produced by the cell, we introduced exogenously prepared Ac-α-syn(A53T) into the biosensor cells using well-established protocols for delivery of proteins via electroporation into mammalian cells (*52-54*) and delivered 70 ± 4 μM of Ac-α-syn(A53T) to these cells (**Figure S5**). To determine if protein delivery by electroporation altered the aggregation of the Ac-α-syn(A53T)-CFP/YFP produced by the biosensor cells, we delivered Ac-α-syn(A53T) and assessed aggregate formation both before and after exposure to fibrils by fluorescence microscopy and cytometry. These cells remained FRET-negative before exposure to fibrils and became FRET-positive only after exposure to fibrils (**Figure S6**). Therefore,

introduction of exogenous Ac-α-syn(A53T) by electroporation does not alter the aggregation behavior of the biosensor cells.

To determine if the introduced Ac-α-syn(A53T) co-localized with Ac-α-syn(A53T)-CFP/YFP produced by the cell, we fluorescently tagged the exogenously prepared protein, delivered it to cells by electroporation, and assessed protein localization by fluorescence microscopy. To do so, we fluorescently labeled Ac-α-syn(A53T) by introducing a cysteine mutation at position 122 (*55*) and attaching a fluorophore (AF^{647}) to the cysteine residue via maleimide chemistry. We then delivered purified monomeric Ac-α-syn(A53T)-AF^{647} to cells by electroporation. After exposure to Ac-α-syn(A53T) fibrils, Ac-α-syn(A53T)-AF^{647} colocalized with the aggregates of Ac-α-syn(A53T)-CFP/YFP produced by the cell (**Figure 3H**). Thus, exogenously prepared Ac-α-syn(A53T) is incorporated into the Ac-α-syn(A53T) fibril-induced aggregates of Ac-α-syn(A53T)-CFP/YFP.

Cells preferentially amplified Ac-α-syn-A53T polymorph B

To determine which amyloid conformations are propagated inside cells, we delivered exogenously prepared Ac-α-syn(A53T) that was specifically isotopically enriched with ^{13}C valine and ^{15}N histidine to the biosensor cells and then exposed the cells to Ac-α-syn(A53T) fibrils. To assess the conformational homogeneity at V49 in the amyloid core, we collected one dimensional NCoCx (*36, 48*) spectra at 104 K on three independently prepared samples. The average signal to noise ratio of these spectra was 8:1 at the V49Cα peak and the SNR of the co-added spectrum was 13:1 (**Figure S7**). In all three repeats, as well as in the co-added spectrum, the peak centers of V49Cβ and V49Cβ' were the same as those of *de novo* fibril seeds, indicating that the same amyloid fibril core structures were present in both samples. In contrast, the relative

populations of these two fibril forms differed. (**Figure 4, Figure S7, Table S4, Table S5**). The population of the major peak in the seeding population decreased from 79% to 33% and the population of the minor peak in the seeding population increased from 21% to 67%; the minority conformation in the seeding population became the majority population when amyloid fibrils were propagated inside cells (**Figure 4A**). Interestingly, the peak center for the Cα was 0.6 ppm larger for the in cell propagated fibrils than the *de novo* fibril seeds (**Figure 4A**). Since the peak centers of V49Cβ and V49Cβ' indicated that the same amyloid fibril core structures were present, the increase in the chemical shift of peak center of the Cα for in cell propagated fibrils indicated that this change was a result of a difference in the chemical shifts of the V49Cα and V49Cα' conformations that is not fully resolved under these experimental conditions. To determine if that was the case, we fit the Cα peak to a sum of two Gaussian peaks and found that fixing the peak center for V49Cα at 60.3 ppm and the peak center for V49Cα' at 61.1 ppm recapitulated not only the change in the Cα chemical shift but also resulted in populations of the V49Cα and V49Cα' peaks that corresponded to the populations of the V49Cβ and V49Cβ' peaks, respectively (**Figure S8, Table S5**). Therefore, the peak centers of the in cell propagated fibrils and the *de novo* fibril seeds were the same. Thus, the same Ac-α-syn(A53T) amyloid core conformations were present in both the seeding and the in cell propagated samples but the relative population of these conformation inverted when amyloid fibrils were amplified in cells.

While the two Ac-α-syn(A53T) amyloid core conformations were present in both the seeding and the in cell propagated samples, the increase in the relative population of the minority population was accompanied by a change in the molecular order of V49Cβ'. The linewidths for the V49Cβ peak were similar for fibrils propagated both *in vitro* and inside cells but the linewidth for the V49Cβ' peak changed dramatically **(Figure 4A, Figure S8**, **Table S5**). The

FWHM for V49Cβ' narrowed from 2.7 ppm for the *de novo* seeds to 1.6 ppm for the in cell propagated fibrils, a linewidth near that of a completely rigid site under these experimental conditions. The peak narrowing indicated that the amyloid cores of Ac-α-syn(A53T) polymorph B fibrils propagated inside cells were more conformationally uniform than those of the *in vitro* assembled fibril. Thus, seeded amplification of Ac-α-syn(A53T) fibrils inside cells resulted in not only an inversion of the population of the polymorphs but also an increase in the molecular order.

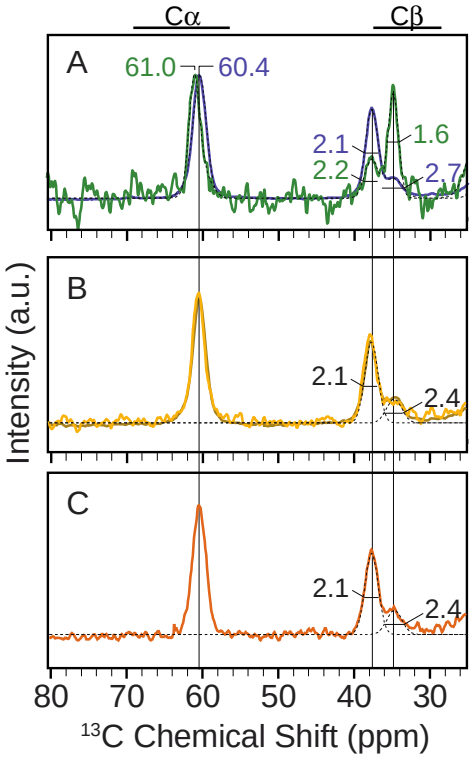

Figure 4*: A) NCOCx of the co-added spectra of in cell propagated ^{13}C valine, ^{15}N histidine labeled Ac-α-syn(A53T) fibrils (green) overlayed with the co-added spectra of the de novo Ac-α-syn(A53T) fibrils used to seed the in cell polymerization (blue). Peak centers are annotated for the V49Cα peak and peak widths as FWHM are annotated for V49Cβ and V49Cβ'peaks. B) The NCOCx spectrum of pre-formed Ac-α-syn(A53T) fibrils diluted into cellular lysates and C) of Ac-α-syn(A53T) fibrils seeded by de novo Ac-α-syn(A53T) fibrils and propagated in cellular lysates.*

Individual Gaussians for V49Cβ and V49Cβ' are shown as black dotted lines. NMR spectra were recorded at a field strength of 14 T (600 MHz) and MAS frequencies of 12 kHz at 104 K.

Crowded cellular lysates fail to recapitulate the preferential amplification of intact cells

To determine if the increase in the population of the minority conformation and the molecular order of the fibril core inside cells was a result of interactions of the amyloid fibrils with cellular constituents, we diluted a small amount of pre-formed isotopically labeled Ac-α-syn(A53T) fibrils into concentrated whole-cell lysates. In these samples, we matched the ratio of the Ac-α-syn-A53T (on a monomer-to-monomer basis) to cells with those in our samples of electroporated biosensor cells so that the stoichiometry of the cellular constituents to fibrils were the same in these two samples. We found that the presence of cellular lysates did not alter the chemical shifts, relative populations, or the peak widths of the 1D NCOCx spectra of V49 in the pre-formed fibrils (**Figure 4B, Table S4**). Therefore, the increase in the population of the minority conformation was not the result of interactions with or remodeling by cellular constituents. Moreover, the higher molecular order of the in cell propagated fibrils was not the result of either binding of cellular constituents or macromolecular crowding.

To determine if the increase in the population of the minority conformation and the molecular order of the fibril core inside cells was a result of amyloid propagation in the presence of cellular constituents and/or macromolecular crowding, we added a small amount (1% monomer/monomer) of pre-formed Ac-α-syn(A53T) fibrils to 70 μM monomeric isotopically labeled Ac-α-syn(A53T) in the presence of concentrated whole-cell lysates, matching the stoichiometry of the in cell propagated fibril samples. We found that the presence of cellular lysates did not alter the chemical shifts, relative populations, or the peak widths of the V49 spectrum of the resulting in lysate propagated fibrils (**Figure 4C, Table S4**). Therefore, neither

interactions with cellular constituents nor macromolecular crowding during amyloid propagation increased either the population of the minority polymorph or the molecular order of the amyloid core. Thus, the selective amplification and the increase in molecular order of the amyloid core required not only the presence of molecular constituents during fibril propagation but also the organization of the molecular constituents found inside intact viable cells.

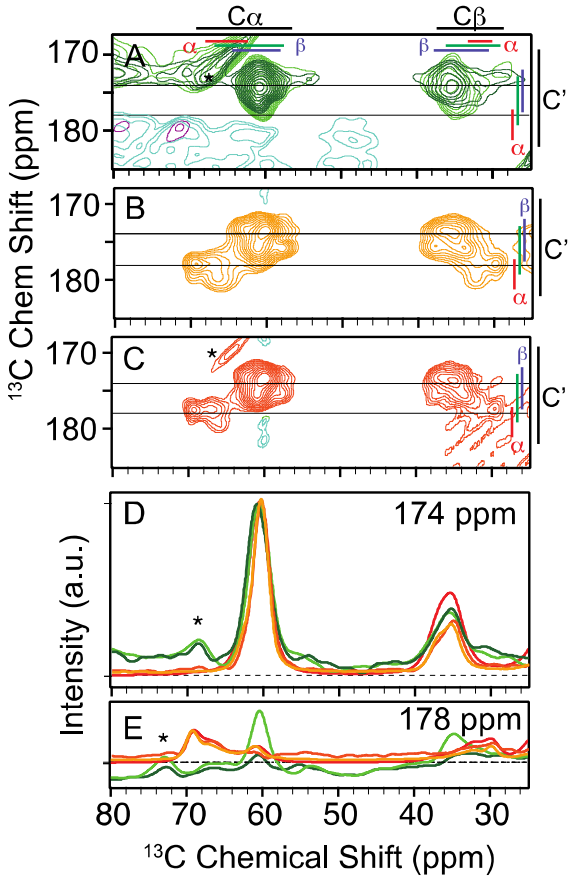

Figure 5: ***A)*** *2D ^{13}C–^{13}C DARR spectra (10 ms mixing) of two independent samples (light green, dark green) of ^{13}C valine labeled Ac-α-syn(A53T) assembled into the amyloid conformation inside intact viable HEK293 cells. Average +/- two standard deviation of the database chemical shift values are marked for each atom (black) as well as for the α-helical (red), random coil (green), and β strand (blue) secondary structural elements.* ***B)*** *2D ^{13}C–^{13}C DARR spectra of pre-formed ^{13}C valine labeled Ac-α-syn(A53T) fibrils diluted in HEK293 cells lysates.* ***C)*** *2D ^{13}C–*

*^{13}C DARR spectra of ^{13}C valine labeled Ac-α-syn(A53T) assembled into the amyloid conformation in HEK293 cells lysates by 1% seeding with sonicated pre-formed fibrils. One-dimensional slices from the 2D spectra of in cell amplified fibrils (dark green, light green), de novo formed amyloid seeds (shown in Figure 1A) (red), pre-formed fibrils diluted into cellular lysates (yellow), and seeded in lysate amplified fibrils (orange) at **D**) 174 ppm and **E**) 178 ppm. Spinning sidebands are marked with a star (*). NMR spectra were recorded at a field strength of 14 T (600 MHz) and a MAS frequency of 12 kHz at 104 K.*

Flanking regions that are intrinsically disordered in purified fibrils are remodeled inside cells

To determine if the conformational preferences of disordered regions that flank the amyloid core are influenced by the cellular environment, we collected a 2D ^{13}C–^{13}C DARR correlation spectrum of ^{13}C valine labeled fibrils that were propagated inside cells as well as pre-formed fibrils that were either diluted into concentrated cellular lysates or propagated in the presence of concentrated cellular lysates and 1% *de novo* seeds. In contrast to the observation of significant cross peak intensity at chemical shifts consistent with α-helical backbone conformations in the spectra of *de novo* fibrils *in vitro* (**Figure 1A, 1D**), there was no cross peak intensity in the α-helical chemical shift region of the 2D ^{13}C-^{13}C DARR spectrum of fibrils that were propagated inside cells (**Figure 5A, 5E**, light and dark green). Yet, the relative cross peak intensity in the α-helical region of the spectra of fibrils that were diluted into **(Figure 5B, 5E**, yellow) or propagated in the presence of cellular lysates **(Figure 5C, 5E**, orange) was similar to that of purified *de novo* formed fibrils (**Figure 1A, 5E**, red). Therefore, the conformational preferences of the valines in the amino terminal region of Ac-α-syn(A53T) fibrils were profoundly altered when the amyloid fibrils were propagated inside intact cells. However, this profound alteration in the conformational preference of the amino-terminal region of Ac-α-syn(A53T) was not the simple consequence of interactions with or remodeling by cellular

constituents, nor of molecular crowding. The alteration in the conformational preferences of the amino terminus required not only the presence of molecular constituents during fibril propagation but also the organization of the molecular constituents found inside intact viable cells during fibril propagation.

Discussion

Amyloid forms of α-syn adopt different conformations depending on environmental conditions. While advances in structural biology have accelerated the characterization of these fibrils, a gap remains in understanding which amyloid conformations are present and their relative prevalence in biological settings because the current methods typically require fibrils to be isolated from their native environments. Thus, the resulting structures may not accurately reflect the ensemble of conformations that exist in cells. Moreover, most approaches do not provide insight into the conformations of the flanking disordered regions. To address these gaps, we use DNP-assisted MAS NMR to investigate the full conformational ensemble of frozen α-syn fibrils in both *in vitro* and biological settings. By relating the NMR spectra of selected sites in frozen α-syn fibrils to the structures we solved by cryo-EM of an *in vitro* sample, we determined the relative populations of the two amyloid polymorphs as well as the conformational preferences of the amino terminal flanking region. We found that the relative populations of the structures and the conformational preferences of the amino terminal flanking region of the Ac-α-syn(A53T) fibril seeds are faithfully amplified in both *in vitro* and in the context of concentrated cellular lysates. However, this is not the case in intact living cells where we found that the minority conformation of the *in vitro* samples became the majority conformation, had higher molecular order, and had altered conformational preferences for the amino terminal region.

Biophysical characterization of the amyloid conformation used to seed fibril polymerization alongside the resulting amyloid forms in different settings indicates that the initial seeding conformations and the amplified conformations sometimes differ (*9, 56, 57*). There are several proposed propagation mechanisms to rationalize these differences. The cloud hypothesis suggests that amyloid fibrils exist as a cloud of conformational variants and different variants are selectively amplified when propagated in different environments (*58, 59*). Deformed templating suggest that when the seeding conformation is amplified in a different environment, it will adopts energetically close but more favorable conformations that differ from the original (*60*). Our quantitative site-specific measurements enable structural characterization of the ensembles of the seeding and the resulting amyloid conformations *in situ.* We establish that both mechanisms are active when *in vitro* formed amyloid fibrils are propagated inside intact cells, albeit at different regions of the protein. When amplified inside intact cells, the amyloid core experiences selective amplification while the amino terminal region in the flanking disordered region experiences deformed templating. Selective amplification of amyloid fibrils inside cells occurs not only at the level of overall amyloid fold, seen though changes in peak intensities, but also at the level of the number of structurally similar conformations that are present in the ensemble, seen through the changes in linewidth. Deformed templating occurs for the amino terminal region, seen through changes in the chemical shifts. Future work will reveal if the changes for fibrils amplified in the context of intact cells result from the alteration of the conformational preferences of a disordered region, the binding of some cellular constituents during amplification, or an extension of the amyloid core.

Understanding the mechanisms that govern *in vitro* amyloid propagation in biological environments will facilitate the development of molecular tools to monitor disease progression.

For example, most structure-based and chemical screens to identify amyloid ligands use *in vitro* amplified α-syn fibrils as the target molecule. Such screens have identified multiple molecules with nanomolar binding affinity to the targeted *in vitro* fibrils (*61-64*). However, none of these compounds interact with α-syn fibrils in brain sections from individuals diagnosed with α-synucleinopathies (*61-65*). Here we found that while both amyloid core conformations present *in vitro* are amplified inside of cells, the amyloid core conformation with less molecular order and a larger buried molecular surface per monomer *in vitro* becomes highly ordered and is selectively amplified inside cells. Thus, ensemble-based experiments can focus structure-based design efforts toward structures that represent the most prevalent conformations in relevant settings.

Structural characterization of *ex vivo* purified fibrils of α-syn and other disease associated amyloid proteins reveal that *ex vivo* fibrils tend to have higher physical stability, larger amyloid cores, and more annotated regions of partial occupancy surrounding the amyloid core in cryo-EM density maps than *in vitro* propagated fibrils. We found that the population of the fibrils propagated inside cells was enriched for the amyloid conformation with the more extensive molecular interface between protofilaments, was more highly ordered, and had changes in the conformational preferences of the amino terminal region from α-helical dihedral angles to those consistent with β-strand and turns relative to the seeding *in vitro* fibrils. Thus, an increase in physical stability is a shared feature of amyloids seeded by *in vitro* fibrils and propagated inside cells that model cytotoxic protein aggregation and *ex vivo* fibrils that are purified from tissues. Interestingly, these more physically robust forms are not the most prevalent for fibrils amplified either *in vitro* or in concentrated cellular lysates, indicating that there are kinetic and/or thermodynamic barriers to accessing the physically more robust forms and that these barriers cannot be trivially overcome by molecular crowding or by addition of cellular constituents

during amplification. The shared physical properties indicate that selective amplification of physically more robust species and ordering of regions that are disordered in purified settings by living cells is a consequence of the organization of the biological constituents found in intact cells and may be a general feature of pathogenic amyloid propagation in cellular environments. The shared properties further indicate that simplified model systems capture not only some of the cytotoxic but also some of the atomistic biophysical features of amyloid aggregation.

Regions of intrinsic disorder are crucial in biology but are challenging to characterize using many biophysical techniques. Here, we characterize disordered regions by freezing the sample to eliminate molecular motions and using solid state MAS NMR. For well-ordered systems, MAS NMR spectra at ambient and cryogenic temperatures show similar line widths (*66*, *67*). The broader line widths typically seen in MAS NMR spectra at cryogenic temperatures come from the freezing out of small excursions around a local minimum. This effect is exaggerated for loops and termini because the spectra report on the chemical shifts of the sampled conformations with peak intensities related to the relative populations of each conformation in the ensemble. Using NMR chemical shifts and peak widths in combination with specific and segmental isotopic labeling of frozen fibril samples, we found that the disordered amino terminal region of α-syn exhibits strong conformational preferences for α-helical dihedral angles *in vitro*. These preferences were unchanged by the presence of cellular constituents or molecular crowding. The strong α-helical preferences of this region could be an artifact of cryogenic conditions or the rate of sample freezing. However, pioneering work to establish the quantitative relationship between conformational ensembles at cryogenic and ambient temperature typically indicates good agreement (*26*-*29*). Moreover, solution-state NMR studies have shown that monomeric α-syn has a propensity for α-helical conformations (*68*), which

increases with amino terminal acetylation (*69*). Furthermore, although there are fewer investigations of the flexible regions that flank the amyloid core because NMR experiments are affected by motions on a variety of timescales, the observable sites have similar conformational preferences to the monomeric form (*70*). Strikingly, these preferences were profoundly altered when amyloid assembly occurred inside cells. This change was not the trivial outcome of interactions with cellular constituents or molecular crowding because the change was not recapitulated by amyloid assembly in concentrated cellular lysates. Thus, features specific to the cellular organization and/or cytotoxic environments can and do alter the conformational preferences of intrinsically disordered regions.

Advances in methods for structural biology coupled with advances in computational protein structure prediction approaches mean that many biological investigations can begin with atomistic structural models of the proteins. The question becomes which models best represent the ensemble of conformations present in the relevant context. While cryo-electron tomography can produce detailed images of macromolecular complexes *in situ,* the resolution of the structures depends upon the ability to precisely identify and overlay multiple images of the same molecule and is limited to measurements on sub-sections of the cellular volume. In contrast, DNP-enhanced NMR can provide direct experimental measurements about the ensemble of conformations adopted *in situ* with atomic-level precision. Although the number of sites that can be unambiguously examined at a single time is limited, quantitative site-specific measurements of the entire structural ensemble can distinguish between structural models of proteins solved in more experimentally tractable settings. Indeed, for problems that require atomic-level information *in situ*, such as the mode of engagement of a small molecule with a target, the spectroscopic view provides unique structural information. Moreover, NMR can provide

structural constraints for the intrinsically disordered regions of proteins which elude characterization by diffraction-based methodologies in both purified and cellular settings. Thus, in cell structural biology aided by DNP-enhanced NMR spectroscopy fills a gap in our ability to study protein conformations *in situ*.

Acknowledgements:

D.L. was supported by NIH MB T32 GM008297. S.K. was supported by UT Dallas and the Cecil and Ida Green Foundation via The Green Fellow's Program. This work was supported by grants from the National Institute of Health [NS111236 and NS134921] to K.K.F. We thank the Structural Biology Laboratory at UT Southwestern Medical Center which is partially supported by grant RP220582 from the Cancer Prevention & Research Institute of Texas (CPRIT) for cryo-EM studies. CEMF is supported by a grant from the Cancer Prevention & Research Institute of Texas (RP220582).

Competing interests: The authors declare that they have no competing interests.

Data and materials availability: The cryo-EM maps have been deposited in the Electron Microscopy Data Bank (EMDB) under accession codes EMD-45650 and EMD-45651. The corresponding atomic coordinates have been deposited in the Protein Data Bank (PDB) under accession codes 9CKK and 9CKL.

Material and Methods

Recombinant protein expression and purification

Protein expression

The genes for the A53T and A53T-N122C mutant form of α-syn in pET28b vector were generated by site-directed mutagenesis using Q5 high fidelity DNA polymerase (New England Biolabs) and mutation was confirmed by DNA sequencing. Amino-terminally acetylated (Ac) α-Syn(A53T) was produced by co-expression of α-syn(A53T) and the yeast N-acetyltransferase complex B (NatB) in *E. Coli* BL21-Gold DE3(Agilent) as described (*71*) (Bell, Rosie, et al.,2022). Co-transfected cells were grown under antibiotic selection (50 µg/mL kanamycin and 34 µg/mL chloramphenicol) with aeration at 37 °C. Natural abundance proteins were expressed on 2xYT media (16 g/L tryptone, 10 g/L yeast extract 5 g/L NaCl). Valine and histidine-labeled proteins were expressed in natural abundance M9 media (48 mM Na_2HPO4, 22 mM KH_2PO4, 9 mM NaCl, adjusted to pH 7.4 by the addition of NaOH, 4 g/L glucose, 1 g/L NH_4Cl, 10 mg/L FeSO4, 2 mM $MgSO_4$, 100 mM $CaCl_2$, 10 mg/L thiamine) supplemented with 100 mg/L of each amino acid except valine and histidine.

Expression of Ac-α-syn(A53T) and Ac-α-syn(A53T-N122C) proteins was induced by the addition of 1 mM Isopropyl β-D-1-thiogalactopyranoside (IPTG) to cells at mid-log phase (OD_{600} of 0.8-1.0). Cells were cultured for 4 hours at 37 °C. For site-specific isotope labeling $^{13}C_5$ valine and $^{15}N_3$ histidine (Cambridge Isotope Laboratories, Tewksbury, MA) isotope-enriched Ac-α-syn(A53T) was expressed in M9 minimal media and added before IPTG induction. Briefly, a preculture of *E.coli* bacterial BL21-Gold DE3 cells with α-syn(A53T) and NatB plasmid was grown overnight at 37°C in 300 mL M9 media supplemented with 4 gm/L glucose, 1 gm/L NH_4Cl, 50 µg/mL Kanamycin and 34 µg/mL chloramphenicol. At the absorbance OD_{600} of 2.2-2.8, cells were collected by centrifugation and washed with 1x M9 salt and resuspended in 1 L fresh M9 minimal media containing natural abundance 4 gm/L glucose, 1 gm/L NH_4Cl and 100 mg/L of all amino acids (Sigma) except valine and histidine. 100 mg/mL of

$^{13}C_5$ valine and $^{15}N_3$ histidine labeled amino acid were added to the above mixture and cells were grown at 37 °C for 90 minutes, followed by induction by addition of 1 mM IPTG at the OD_{600} of 0.8-1.0. After 4 hours, cells were collected by centrifugation at 4000 x g for 20 minutes and stored at -80 °C.

Purification

Purification was performed as described previously (Kloepper, K. D. et al. 2006. , (*29*). Briefly, pelleted cells were resuspended in 160 mL of lysis buffer (20 mM Tris, 1 mM EDTA and 0.1% Triton X, pH 8.0) and incubated at 37 °C in the water bath. After 30 minutes, 800 µL of 2 M $MgCl_2$ and 1.6 mL 1 M $CaCl_2$ were added to the lysed cells along with 2.5 µL DNase (New England Biolabs) and OmniCleave endonuclease (Biosearch Technology) for nucleic acid digestion. This mixture was incubated at 37 °C for 1 hour with shaking at 200 rpm. Afterward, 1.6 mL of 0.5 M EDTA was added to the mixture to remove excess metal. Cell suspension was centrifugated at 4200 x g for 15 minutes, and 6 parts of the supernatant were mixed with 1 part of 5 M NaCl and boiled for 15 minutes in the water bath. Following another 20-minute centrifugation at 30000 x g, an equal volume of saturated ammonium sulphate (50% *v/v*) was added to the supernatant and the solution was stirred overnight at 4 °C. The precipitated Ac-α-syn(A53T) was resuspended in buffer A (20 mM NaCl, 20 mM Tris, pH 8.0). The whole mixture was dialyzed for 16-20 hours against 4 L buffer A. The dialyzed solution was filtered with 0.22 µM filter (Corning) and loaded on to a Q-Sepharose column (GE healthcare), that was pre-equilibrated with buffer A. Ac-α-syn(A53T) protein fractions were eluted with a gradient (0-80%) of buffer B (20 mM Tris, 2 M NaCl, pH 8.0). Fractions containing α-syn were concentrated to ~1 mM with an Amicon centrifugal filter (Millipore, Sigma) and injected to superdex 75 hi-scale 26/40 size exclusion column (GE healthcare). Pure monomeric Ac-α-syn(A53T) protein

fractions were pooled and purity was determined by 10% sodium dodecyl sulphate polyacrylamide gel electrophoresis (SDS-PAGE). All chromatography was performed on the Biorad NGC chromatography system (Biorad). Protein concentration was determined by UV absorption at 280 nm using a theoretical extinction coefficient of 5960 M^{-1} cm^{-1}. Acetylation and protein molecular weight were confirmed by LC/MS with a Q-TOF mass spectrometer.

Segmentally isotopically labeled protein expression and purification

To express isotopically-labeled recombinant N^{α}-acetylated α-syn(1-29)-Cfa_N construct, an overnight pre-culture of BL21(DE3) cells carrying simultaneous plasmids encoding α-syn(1-29)-Cfa_N and yeast NatB was used to inoculate 4 liters of M9 media with $^{13}C_5$-valine was added at a final concentration of 100 mg/L containing 50 mg/L kanamycin and 34 mg/L chloramphenicol.. Cells were grown at 37 °C with shaking until their A_{600} reached 0.6–0.8; the protein expression was then induced by adding isopropyl 1-thio-β-D-galactopyranoside (IPTG) to a final concentration of 1 mM. Cells were harvested 4 hours after induction by centrifugation at 4000 × *g* for 15 min at 4 °C.

Natural-abundance recombinant Cfa_C-α-syn(C30-140, A53T) was expressed in LB media (10 g/L tryptone, 5 g/L yeast extract, 10 g/L NaCl). Cells were grown at 37 °C with shaking until their A_{600} reached 0.6–0.8, and protein expression was induced by the addition of IPTG to a final concentration of 1 mM. Cells were collected 4 h later by centrifugation at 4,000 × *g* for 15 min at 4 °C.

Proteins from constructs 1 and 2 were purified using nickel resin. Cell pellets were lysed by resuspension in 20 mL of binding buffer (100 mM NaH_2PO_4, 500 mM NaCl, 4 mM TCEP, pH 8.0) per liter of growth. Protease inhibitor tablets were added. The cell suspension was sonicated 6 times (pulse: 60% amplitude, 30 s, 0.5 s on, 0.5 s off). Lysates were centrifuged for 20 min at

30,000 × *g* to remove insoluble cellular debris. Cleared lysates were filtered using 0.2 µM filter then passed through a 15-mL Nickel column using Biorad NGC system. The column was washed with 10-15 column volumes (CV) of binding buffer (100 mM NaH_2PO_4, 500 mM NaCl, 2 mM TCEP, pH 8.0). It was then washed with 10-15 CV of wash buffer (100 mM NaH_2PO_4, 500 mM NaCl, 10 mM imidazole, 2 mM TCEP, pH 8). The protein was eluted in elution buffer (100 mM NaH_2PO_4, 500 mM NaCl, 450 mM imidazole, 2 mM TCEP, pH 8). Purity was assessed by SDS/PAGE. Protein concentration was quantitated using theoretical extinction coefficients of 26930 $M^{-1}{\cdot}cm^{-1}$ for construct 1 and 7450 $M^{-1}{\cdot}cm^{-1}$ for construct 2.

Split-Intein Ligation and Purification

The purified split-intein constructs were ligated at room temp overnight with a molar excess of 1:1.5 (construct 1:construct 2) in ligation buffer [50 mM Tris, 300 mM NaCl, 2 mM Tris(2-carboxyethyl)phosphine (TCEP), 0.5 mM EDTA, pH 7.4]. The final concentrations of constructs 1 and 2 were 25 µM and 30 µM, respectively. The reaction mixture was left at 4 °C overnight. It was then concentrated 5-fold using a 10-kDa molecular mass cutoff Amicon spin concentrator. The reaction mixture was then incubated with Ni-NTA resin for an hour at room temperature. The resin was transferred to a PD-10 column and washed with 1 CV of binding buffer. The flowthrough and the wash were collected since they contain the Ac-α-syn(A53T) that is untagged. The protein solution was concentrated 10-15 fold before proceeding to the desulfurization step.

Desulfurization was done following a previously published protocol, which contains important safety precautions (*72*). Briefly, pH-adjusted TCEP was added to the protein solution to bring up the concentration of TCEP to 100 mM. Then the radical initiator solution (100 mM

VA-044 in 6 M guanidine hydrochloride, 50 mM sodium phosphate, pH 7.2) was added to a final concentration of 6 mM. The following steps are all done in a fume hood. Methylpropane-2-thiol (or t-butyl mercaptan) was added in the hood to a final concentration of 400 mM. The reaction was left on an orbital shaker for 2 hours at 600-800 rpm at 37 °C. The protein was then isolated in the hood using PD10 columns equilibrated with the buffer of interest.

At this step we had Ac-α-syn(A53T) and an 11-kDa byproduct of the ligation reaction (the last 111 amino acids of synuclein). Therefore, after the desulfurization reaction, the protein was concentrated and loaded onto a Superdex 75 size exclusion column. The fractions containing isolated full-length Ac-α-syn(A53T) were pooled together.

Maleimide Labeling of Ac-α-syn(A53T- N122C)

Alexa fluor 647 maleimide (AF^{647}) (Invitrogen) was site-specifically attached to Ac-α-syn(A53T- N122C) protein at position 122. Before labeling with AF^{647}, the protein was incubated in degassed labeling buffer (100 mM $NaHPO_4$, 5 mM KCl, 15 mM HEPES, pH 7.0) with a 10-fold excess of TCEP (Gold Biotechnology). The excess of TCEP was removed by filtration over a NAP-10 column (Sephadex G-25, Cytiva). The maleimide dye was added to the protein at a 4:1 molar ratio and the reaction mixture was incubated in the dark at 25 °C for 4 h. The labeling reaction was quenched by addition of excess of β-mercaptoethanol and free fluorophore was removed by using a PD-10 desalting column (Cytiva). The labeling efficiency was calculated as described (*73*) and samples were concentrated with Amicon centrifugal filters.

Preparation of *in vitro* fibrils

Ac-α-syn(A53T) *de novo* fibrils were prepared as described (*46*). Briefly, monomeric protein was diluted to 300 μM in Dulbecco's phosphate-buffered saline (DPBS, Gibco) and

incubated at 37 °C for 5 days with constant agitation at 1000 rpm in an Eppendorf orbital thermomixer. First generation fibrils were prepared by adding 1% (*mol/mol*) of *de novo* fibrils to the monomer at the start of the polymerization reaction. For DNP NMR studies, fibrils were collected by centrifugation at 200,000 x g for 1 hour and the supernatant was removed. The pellet was resuspended in perdeuterated 1x PBS buffer containing a final composition of either 60% d_8-glycerol, 30% D_2O, 10% H_2O pH 7.4, and 7 mM AMUPol or 15% d_8-glycerol, 75% D_2O,10% H_2O pH 7.4 and 7 mM AMUPol. The sample was packed into a 3.2 mm sapphire rotor (Bruker) and stored at -80 °C.

Transmission electron microscopy

Ac-α-syn(A53T) fibril samples (5 μL) were loaded onto a glow-discharged carbon-coated electron microscopy grid. After 1 min, the grid was washed 3 times with 5 μL distilled water and 5 μL uranyl acetate (2% in aqueous solution) was applied to the grid for 1 min. Filter paper was used to remove excessive stains. The samples were imaged using an FEI Tecnai G2 Spirit Biotwin electron microscope.

Cryo-EM sample preparation and data acquisition

The Ac-α-syn(A53T) fibril sample was the applied to Quantifoil 300-mesh R1.2/1.3 grids (Quantifoil, Micro Tools GmbH, Germany) that were pre-treated using a Pelco EasiGlow instrument (Ted Pella). The grid was flash-frozen into liquid ethane using a Vitrobot Mark IV (Thermo Fisher Scientific), with the following settings: blot time 3.5 s, relative humidity 95%, and 4 °C.

Grid screening and data collection were performed at the UTSW Cryo-Electron Microscopy Facility (CEMF). After screening, the best grid was used for a 24-hour data

collection on a Titan Krios microscope (Thermo Fisher Scientific) equipped with the post-column BioQuantum energy filter (Gatan) and a K3 direct electron detector (Gatan). Cryo-EM data were collected using SerialEM (*74*) in a super-resolution mode with a 20 eV energy filter slit in CDS mode. 7020 movies were acquired in super-resolution mode, at a pixel size of 0.42 Å. The accumulated total dose was 50 $e^-/Å^2$ for each movie stack and it was fractionated into 50 frames. The defocus range of the images was set to be −0.9 to −2.2 μm.

Cryo-EM data processing

Cryo-EM data were processed using Relion (*75-77*). Motion correction was performed using MotionCor2 (*78*) and the movies were averaged into single images with a binning factor of 2, resulting in a pixel size of 0.84 Å/pixel. The CTF parameters were calculated using Gctf (*79*). Fibril auto-picking was done using Topaz (*80*) within the Relion pipeline, and 2,266,580 particles were extracted at 800 box size with an inter-box distance of 38 Å, down sampled to 2.52 Å/pixel for 2D classification. Two types of fibrils were observed in the 2D classes based on the distinct features. The crossover distance for each fibril type was estimated from the 2D classes and was used in relion_helix_inimodel2d to generate the initial model. For Polymorph A, 813,225 particles were selected and re-extracted at 300 box size, followed by 3D classification, 3D refinement, and CTF refinement. 85,236 particles were used to reconstruct the final density map, and the reported resolution was 2.21 Å by Relion post-processing. The polymorph A fibril structure adopts a $C2_1$ screw symmetry. The refined helical twist is 179.61 degrees, and the helical rise is 2.40 Å. For polymorph B, 983,759 particles were selected and re-extracted at 300 box size. After multiple rounds of 3D classification, 11,326 particles were selected for 3D refinement to generate the final density map. The resolution of this map was 2.68 Å as estimated

by Relion post-processing. Polymorph B structure adopts a C2 symmetry. The refined helical twist is -1.21 degrees, and the helical rise is 4.81 Å.

Model building and refinement

For both Polymorph A and Polymorph B structures, an initial model was first built using Model Angelo (*81*) in the Relion pipeline, followed by manual building in Coot (*82*) and Chimera (*83*). The models were then refined with Phenix Real-space refinement (*84*). The statistics of the model validations are summarized in Table S2.

Cellular NMR sample preparation

To introduce isotopically labeled α-syn(A53T) into mammalian cells, we used a modified protocol based on previous work (*41*). HEK293T α-syn(A53T)-CFP/YFP biosensor cell lines were grown in DMEM (Gibco) with 10% FBS (Gibco) and 0.5% GlutaMAX (Gibco) at 37 °C in 5% CO_2 humidified incubator on a 10 cm dish to confluency. Cells were washed with 1x PBS (Gibco) and harvested using Tryp-LE express (Gibco). 48×10^6 cells were collected by centrifugation (233 x g, 5 min) and resuspended in 1 mL electroporation buffer (EPB) 100 mM $NaHPO_4$, 5 mM KCl, 15 mM HEPES, 15 mM $MgCl_2$, 2 mM reduced glutathione and 2 mM ATP, pH 7.0. Cells suspension in EPB were collected by centrifugation at 233 x g for 5 min and supernatant was discarded. Cell pellets (~48×10^6 cells) were resuspended in 1.1 mL EPB containing a final concentration of 800 μM monomeric α-syn(A53T). α-syn(A53T) was introduced into cells by electroporation. 100 μL aliquots of the cells and α-syn(A53T) mixture in EPB were transferred to electroporation cuvettes (Lonza) and electroporation was done on the Lonza 4D nucleofector system by using the CM-130 pulse program. Cells were pulsed two times

and gently mixed between the pulses. After electroporation, 500 µL of cell culture media was added to each cuvette and mixed with the cells using a Pasteur pipette and all electroporated cells were added to 10 mL of prewarmed cell culture medium in a 100 mm diameter dish (Corning) and incubated for 5 hours at 37°C with 5% CO_2.

Seeding

After electroporated cells recovered for 5 hours, adherent cells were rinsed with 1 x PBS and detached using Tryp-LE express. For in cell seeding, fibrils were sonicated for 15 minutes at 4 °C in a water bath using an ultrasonicator (QSonica, Q700) with pulses of 3 sec on/2 sec off and 30% amplitude. Sonicated Ac-α-syn(A53T) fibrils (11.5 µL, 100 µM) were diluted in 738 µl of Opti-MEM. In the second tube, 30 µl of Lipofectamine (Invitrogen, 11668019) was added with 720 µl of Opti-MEM and incubated at RT for 5 minutes. The 1.5 mL mixture of fibrils and lipofectamine was incubated at RT for 30 minutes before dropwise addition to the cell suspension (4-4.5 x 10^6 cells) in 10 mL DMEM media with 10% FBS and 1% Penicillin-Streptomycin. The final concentration of the sonicated Ac-α-syn(A53T) fibrils was 100 nM. Cells were incubated at 37 °C with 5% CO_2 and harvested after 24 hours.

Microscopy

For microscopy, samples were treated identically except that Ac-α-syn(A53T-N122C)-AF^{647} was introduced into cells at the electroporation step instead of Ac-α-syn(A53T). After the 24-hour incubation step, cells were washed with 1x dPBS (Thermofisher, 14040133) and stained with 2.5 µg/mL cell mask orange plasma membrane stain (Invitrogen, C10045) for 5 min at 37 °C. Cells were quickly washed 3 times with cold 1x dPBS and fixed in 4 % (*w/v*) paraformaldehyde (PFA) for 15 minutes at room temperature. After washing once in 1x dPBS

cells were stored in 1x live cell imaging solution (Invitrogen, A59688DJ) for microscopy. Confocal images were taken at 63x magnification on a Zeiss LSM 880 Confocal Microscope by using the excitation wavelengths of 405, 561, and 633 nm for CFP, cell mask orange and AF^{647} respectively. Images were analyzed using Fiji software.

FRET experiments

For the FRET seeding assay, cells were harvested after 24 hours and fixed with 2% paraformaldehyde (Electron Microscopy Sciences) for 10 minutes. After centrifugation cell pellet was resuspended in 2 mL cold 1x PBS for flow cytometry analysis. Three additional control cell lines (HEK293T cells, α-syn(A53T)-YFP and α-syn(A53T)-CFP transduced cells) were used in this assay. The sample was analyzed by LSRII Fortessa flow cytometer (BD Biosciences), where the FRET signal was detected using the CFP-specific 405 nm laser with 525/50 bandpass filter. CFP and YFP are excited by 405 nm and 488 nm lasers with 450/50 and 525/50 nm bandpass filters, respectively. For sorting, cells were seeded with 100 nM Ac-α-syn(A53T) fibril for 24 h and harvested. Cells pellet mixed with 1 mL cold Flow buffer (1X Hank Balanced salt solution, Ca^{++}/Mg^{++} free, 1% FBS and 1 mM EDTA) and filtered through cellTrics filter (Sysmex). FRET negative and positive cells were sorted at 4 °C using FACSArias by using the CFP-specific 405 nm laser with a 525/50 bandpass filter.

Growth Assay

600,000 cells were plated in 10 cm dishes containing 10 mL warm media (DMEM). Media was changed after cells had adhered overnight and cells were incubated for 4-5 days. Confluency was monitored daily at 3 independent areas of each dish with an inverted light microscope (Olympus CKX53 Tokyo, Japan). Confluency was determined using ImageJ.

Annexin-PI assay

The Annexin V-Alexa Fluor 647 conjugate and propidium iodide (PI, Invitrogen) combination was employed to quantitate apoptosis following the manufacturer's instructions. Briefly, cells were seeded with 100 nM Ac-α-syn(A53T) *de novo* fibril and incubated for 24-72 h. Post-treatment, cells in 10 mL culture media were stained with 2.5 μL annexin V-Alexa Fluor 647 and 1 μL PI for 15 min in the dark before cytometry analysis with a LSRII Fortessa flow cytometer (BD Biosciences). The FRET signal was detected using CFP specific 405 nm laser with a 525/50 bandpass filter. We plotted the FRET versus CFP bivariate plot and introduced a gate to separate the FRET-positive and negative cell populations. To detect apoptosis in the FRET positive population, Annexin V-Alexa Fluor 647 and PI fluorescence emission was measured using the 670/20 nm bandpass and 660/20 long-pass filter with excitation wavelengths of 633 and 532 nm, respectively. A total of 30,000 events per sample were recorded, and compensation was set up using unstained cells and cells stained with a single-color dye only. Data were analyzed using FlowJo 10.9.0 software.

NMR sample preparation of in cell propagated fibril

For the intact cell sample, pelleted cells were washed with 1 mL of perdeuterated 1x PBS (88% D_2O, 10% H_2O, pH 7.4). After centrifugation (233 x g, 5 min), the 50 μL cell pellet was mixed with 50 μL of perdeuterated 1x PBS containing AMUPol (Cortecnet, USA) and 18 μL d_8-^{13}C-depleted glycerol (Cambridge Isotope Labs). The 118 μL cell suspension had a final sample matrix of 15:75:10 d_8-^{13}C-depleted glycerol:D_2O:H_2O (*v*/*v*/*v*) with 5 mM AMUPol. Cells were packed in a 3.2 mm sapphire rotor (Bruker) by centrifugation at 100 x g for 1 min. The rotor was sealed with a silicone plug and capped with a zirconia drive cap. The rotor was frozen for 6 hours

at a controlled rate of 1 °C/min in "Cool Cell LX" (Corning) in the −80 °C freezer before transfer to liquid nitrogen until NMR analysis.

The fibril-containing fraction of one sample of in cell propagated fibrils was increased to improve sample signal to noise. To do so, pelleted cells were resuspended in 500 µL of perdeuterated 1x PBS (88% D_2O, 10% H_2O pH 7.4). Cells were lysed in 500 µL buffer by three freeze-thaw cycles in liquid nitrogen. The insoluble high molecular weight cellular material was collected by centrifugation at 200,000 x g for 10 minutes. The 25 µL pellet was mixed with 25 µL of perdeuterated 1x PBS containing AMUPol (Cortecnet, USA) and 9 µL d_8-^{13}C-depleted glycerol. The insoluble portion was collected in a 3.2 mm rotor and the final sample composition was 15:75:10 d_8-glycerol:D_2O:H_2O (*v*/*v*/*v*) with 5 mM AMUPol.

For the dilution of pre-formed VH-labeled Ac-α-syn(A53T) fibrils into cellular lysates, 50 µL cell pellet lysate having fibril was mixed with 50 µL of perdeuterated 1x PBS (85% D_2O + 10% H_2O, pH 7.4) containing AMUPol (Cortecnet, USA) and 18 µL of d_8-^{13}C-depleted-glycerol. The 118 µL cell suspension had a final composition of 23 µM fibril, 5 mM AMUPol with 15% (*v*/*v*) d_8-^{13}C-depleted-glycerol, 75% (*v*/*v*) D_2O, and 10% (*v*/*v*) H_2O.

For the seeding amplification of VH-labeled Ac-α-syn(A53T) monomer in cellular lysates of sensor cells that had never been exposed to amyloid fibrils, a 50 µL cell pellet was lysed by three freeze thaw cycles in the presence of 1x protease inhibitor (Sigma-Aldrich, 11836170001) and VH-labeled Ac-α-syn(A53T) monomer was diluted into the lysate to a concentration of 75 µM. Sonicated, pre-formed VH-labeled Ac-α-syn(A53T) fibrils were added at a calculated monomer concentration of 1% (0.75 µM) relative to the exogenously added Ac-α-syn(A53T) (~0.3% relative to total α-syn content of the sample). The mixture was incubated for 24 hours at

37 °C in a 5% CO_2 atmosphere. After incubation, we added 500 µL of perdeuterated 1x PBS (85% D2O + 10% H2O, pH 7.4) to the sample and collected the insoluble high molecular weight cellular material by centrifugation at 200,000 x g for 10 minutes. The ~25 µL pellet was mixed with 25 µL of perdeuterated 1x PBS containing AMUPol (Cortecnet, USA) and 9 µL d_8-^{13}C-depleted glycerol and transferred to a 3.2 mm rotor. The final sample composition was 15:75:10 d_8-^{13}C-depleted glycerol:D_2O:H_2O (*v/v/v*) with 5 mM AMUPol.

NMR Spectroscopy

Rotors were transferred in liquid nitrogen directly into the NMR probe that had been previously equilibrated to 100 K (*37*). All dynamic nuclear polarization magic angle spinning nuclear magnetic resonance (DNP MAS NMR) experiments were performed on a 600 MHz Bruker Ascend DNP NMR spectrometer/7.2 T Cryogen-free gyrotron magnet (Bruker), equipped with a ^{1}H, ^{13}C, ^{15}N triple-resonance, 3.2 mm low temperature (LT) DNP MAS NMR Bruker probe (600 MHz). The sample temperature was 104 K and MAS frequency was 12 kHz. For ^{13}C cross-polarization (CP) MAS experiments, the ^{13}C radio frequency (RF) amplitude was fixed at 60 kHz and an ^{1}H RF amplitude was 72 kHz. The 90° ^{1}H pulse was 100 kHz, the 90° ^{13}C pulse was 62.5 kHz, and ^{1}H TPPM at 85 kHz for decoupling with phase alternation of ± 15° during acquisition of ^{13}C signal. ^{13}C-^{13}C 2D correlations were measured using 10 ms DARR mixing with the ^{1}H amplitude at the MAS frequency. A total of 280 points in the indirect dimension were recorded with an increment of 25 µs. DARR experiments were apodized with a Lorenz-to-Gauss window function with IEN of 25 Hz and GB of 75 Hz in the t_1 and t_2 time domains. The noise level and peak height from the 2D NMR spectrum was detected by the NMRDraw software for signal-to-noise estimation. For NCOCX double CP experiment, the first CP was applied with ^{1}H RF amplitude linearly swept from 51 to 101 kHz and ^{15}N amplitude at 40 kHz, at a 1.8 ms

contact time. The second CP was applied with an upward tangential ramp for ^{13}C (tan50) RF amplitude from 24 kHz to 36 kHz, ^{15}N amplitude at 42 kHz, and ^{1}H constant wave decoupling at 98 kHz, at a 6 ms contact time. The spin diffusion was applied with ^{1}H constant wave RF amplitude at 12 kHz for 50 ms.

Gaussian fitting for 1D NCOCx spectrum:

For fitting of 1D NCOCx experiments, the data were processed using NMRPipe. The real part of the processed spectrum was exported using pipe2txt.tcl command. A sum of four Gaussian functions was used to fit the NCOCx spectra. The Gaussian function is defined as:

$$y_i = A_i \exp\left(-0.5\left(\frac{x-\mu_i}{\sigma_i}\right)^2\right)$$

where A_i is the amplitude, μ_i is the mean, and σ_i is the standard deviation of the i-th Gaussian function. A constant offset c was included to account for baseline correction. The total fitting function is given by:

$$y = y_1 + y_2 + y_3 + y_4 + c$$

An initial guess for the parameters was inputted, and the lower and upper bounds for the parameters were set to constrain the optimization process. The built-in MATLAB function 'lsqcurvefit' was used to fit the Gaussian functions to the data. The peak centers for the Cα and Cα' peaks were fixed at 61.1 and 60.3 ppm, respectively, while the peak centers for the Cβ and Cβ' peaks were allowed to vary.

References cited:

1. M. Schweighauser *et al.*, Structures of alpha-synuclein filaments from multiple system atrophy. *Nature* **585**, 464-469 (2020).
2. L. Frey *et al.* (eLife Sciences Publications, Ltd, 2024).
3. S. Lovestam, S. H. W. Scheres, High-throughput cryo-EM structure determination of amyloids. *Faraday Discuss* **240**, 243-260 (2022).
4. J. P. Seibyl, alpha-Synuclein PET and Parkinson Disease Therapeutic Trials: Ever the Twain Shall Meet? *J Nucl Med* **63**, 1463-1466 (2022).
5. S. J. Wood *et al.*, alpha-synuclein fibrillogenesis is nucleation-dependent. Implications for the pathogenesis of Parkinson's disease. *J Biol Chem* **274**, 19509-19512 (1999).
6. H. Miake, H. Mizusawa, T. Iwatsubo, M. Hasegawa, Biochemical characterization of the core structure of alpha-synuclein filaments. *J Biol Chem* **277**, 19213-19219 (2002).
7. M. D. Tuttle *et al.*, Solid-state NMR structure of a pathogenic fibril of full-length human alpha-synuclein. *Nat Struct Mol Biol* **23**, 409-415 (2016).
8. C. Kim *et al.*, Exposure to bacterial endotoxin generates a distinct strain of α-synuclein fibril. *Sci Rep* **6**, 30891 (2016).
9. C. Peng *et al.*, Cellular milieu imparts distinct pathological α-synuclein strains in α-synucleinopathies. *Nature* **557**, 558-563 (2018).
10. F. De Giorgi *et al.*, Novel self-replicating α-synuclein polymorphs that escape ThT monitoring can spontaneously emerge and acutely spread in neurons. *Sci Adv* **6**, (2020).
11. A. Tarutani, T. Arai, S. Murayama, S.-i. Hisanaga, M. Hasegawa, Potent prion-like behaviors of pathogenic α-synuclein and evaluation of inactivation methods. *Acta Neuropathologica Communications* **6**, 29 (2018).
12. Y. Yang *et al.*, Structures of alpha-synuclein filaments from human brains with Lewy pathology. *Nature*, (2022).
13. Y. Yang *et al.*, New SNCA mutation and structures of α-synuclein filaments from juvenile-onset synucleinopathy. *Acta Neuropathologica* **145**, 561-572 (2023).
14. M. Zielinski, C. Röder, G. F. Schröder, Challenges in sample preparation and structure determination of amyloids by cryo-EM. *J Biol Chem* **297**, 100938 (2021).
15. D. D. Dhavale *et al.*, Structure of alpha-synuclein fibrils derived from human Lewy body dementia tissue. *Nat Commun* **15**, 2750 (2024).
16. X. Yang, B. Wang, C. L. Hoop, J. K. Williams, J. Baum, NMR unveils an N-terminal interaction interface on acetylated-α-synuclein monomers for recruitment to fibrils. *Proceedings of the National Academy of Sciences* **118**, e2017452118 (2021).
17. P. Kumari *et al.*, Structural insights into α-synuclein monomer–fibril interactions. *Proceedings of the National Academy of Sciences* **118**, e2012171118 (2021).
18. A. Peduzzo, S. Linse, A. K. Buell, The Properties of α-Synuclein Secondary Nuclei Are Dominated by the Solution Conditions Rather than the Seed Fibril Strain. *ACS Chem Neurosci* **11**, 909-918 (2020).
19. S. F. Falsone *et al.*, SERF protein is a direct modifier of amyloid fiber assembly. *Cell Rep* **2**, 358-371 (2012).
20. X. Gao *et al.*, Human Hsp70 Disaggregase Reverses Parkinson's-Linked α-Synuclein Amyloid Fibrils. *Mol Cell* **59**, 781-793 (2015).
21. D. Cox *et al.*, The small heat shock protein Hsp27 binds α-synuclein fibrils, preventing elongation and cytotoxicity. *J Biol Chem* **293**, 4486-4497 (2018).

22. E. M. Martin *et al.*, Conformational flexibility within the nascent polypeptide-associated complex enables its interactions with structurally diverse client proteins. *J Biol Chem* **293**, 8554-8568 (2018).
23. B. M. Burmann *et al.*, Regulation of α-synuclein by chaperones in mammalian cells. *Nature* **577**, 127-132 (2020).
24. S. D. Khare, P. Chinchilla, J. Baum, Multifaceted interactions mediated by intrinsically disordered regions play key roles in alpha synuclein aggregation. *Current Opinion in Structural Biology* **80**, 102579 (2023).
25. S. M. Ulamec, D. J. Brockwell, S. E. Radford, Looking Beyond the Core: The Role of Flanking Regions in the Aggregation of Amyloidogenic Peptides and Proteins. *Frontiers in Neuroscience* **14**, (2020).
26. R. H. Havlin, R. Tycko, Probing site-specific conformational distributions in protein folding with solid-state NMR. *Proceedings of the National Academy of Sciences* **102**, 3284-3289 (2005).
27. K. N. Hu, R. H. Havlin, W. M. Yau, R. Tycko, Quantitative determination of site-specific conformational distributions in an unfolded protein by solid-state nuclear magnetic resonance. *J Mol Biol* **392**, 1055-1073 (2009).
28. B. Uluca *et al.*, DNP-enhanced MAS NMR: a tool to snapshot conformational ensembles of α-synuclein in different states. *Biophysical journal* **114**, 1614-1623 (2018).
29. J. Kragelj, R. Dumarieh, Y. Xiao, K. K. Frederick, Conformational ensembles explain NMR spectra of frozen intrinsically disordered proteins. *Protein Sci*, e4628 (2023).
30. K. K. Frederick *et al.*, Sensitivity-enhanced NMR reveals alterations in protein structure by cellular milieus. *Cell* **163**, 620-628 (2015).
31. W. N. Costello, Y. Xiao, K. K. Frederick, DNP-Assisted NMR Investigation of Proteins at Endogenous Levels in Cellular Milieu. *Methods Enzymol* **615**, 373-406 (2019).
32. S. Narasimhan *et al.*, DNP-Supported Solid-State NMR Spectroscopy of Proteins Inside Mammalian Cells. *Angew Chem Int Ed Engl* **58**, 12969-12973 (2019).
33. D. Beriashvili *et al.*, A high-field cellular DNP-supported solid-state NMR approach to study proteins with sub-cellular specificity. *Chemical Science* **14**, 9892-9899 (2023).
34. R. Ghosh, Y. Xiao, J. Kragelj, K. K. Frederick, In-Cell Sensitivity-Enhanced NMR of Intact Viable Mammalian Cells. *J Am Chem Soc* **143**, 18454-18466 (2021).
35. J. Kragelj *et al.*, Spatially resolved DNP-assisted NMR illuminates the conformational ensemble of α-synuclein in intact viable cells. *bioRxiv*, 2023.2010.2024.563877 (2023).
36. W. N. Costello, Y. Xiao, F. Mentink-Vigier, J. Kragelj, K. K. Frederick, DNP-assisted solid-state NMR enables detection of proteins at nanomolar concentrations in fully protonated cellular milieu. *Journal of Biomolecular NMR*, (2024).
37. R. Ghosh, J. Kragelj, Y. Xiao, K. K. Frederick, Cryogenic Sample Loading into a Magic Angle Spinning Nuclear Magnetic Resonance Spectrometer that Preserves Cellular Viability. *J Vis Exp*, (2020).
38. Y. Xiao, R. Ghosh, K. K. Frederick, In-Cell NMR of Intact Mammalian Cells Preserved with the Cryoprotectants DMSO and Glycerol Have Similar DNP Performance. *Front Mol Biosci* **8**, 789478 (2021).
39. R. Ghosh, R. Dumarieh, Y. Xiao, K. K. Frederick, Stability of the nitroxide biradical AMUPol in intact and lysed mammalian cells. *J Magn Reson* **336**, 107150 (2022).
40. D. W. Sanders *et al.*, Distinct tau prion strains propagate in cells and mice and define different tauopathies. *Neuron* **82**, 1271-1288 (2014).

41. F. X. Theillet *et al.*, Structural disorder of monomeric alpha-synuclein persists in mammalian cells. *Nature* **530**, 45-50 (2016).
42. A. L. Woerman *et al.*, Propagation of prions causing synucleinopathies in cultured cells. *Proceedings of the National Academy of Sciences* **112**, E4949-E4958 (2015).
43. S. B. Prusiner *et al.*, Evidence for α-synuclein prions causing multiple system atrophy in humans with parkinsonism. *Proceedings of the National Academy of Sciences* **112**, E5308-E5317 (2015).
44. A. L. Woerman *et al.*, MSA prions exhibit remarkable stability and resistance to inactivation. *Acta Neuropathologica* **135**, 49-63 (2018).
45. J. Chlebowicz *et al.*, Saturation mutagenesis of α-synuclein reveals monomer fold that modulates aggregation. *Science Advances* **9**, eadh3457 (2023).
46. Y. Sun *et al.*, Cryo-EM structure of full-length α-synuclein amyloid fibril with Parkinson's disease familial A53T mutation. *Cell Res* **30**, 360-362 (2020).
47. J. I. Ayers *et al.*, Different alpha-synuclein prion strains cause dementia with Lewy bodies and multiple system atrophy. *Proc Natl Acad Sci U S A* **119**, (2022).
48. J. Pauli, M. Baldus, B. van Rossum, H. de Groot, H. Oschkinat, Backbone and Side-Chain 13C and 15N Signal Assignments of the α-Spectrin SH3 Domain by Magic Angle Spinning Solid-State NMR at 17.6 Tesla. *ChemBioChem* **2**, 272-281 (2001).
49. Y. Wang, O. Jardetzky, Probability-based protein secondary structure identification using combined NMR chemical-shift data. *Protein Sci* **11**, 852-861 (2002).
50. M. V. Berjanskii, S. Neal, D. S. Wishart, PREDITOR: a web server for predicting protein torsion angle restraints. *Nucleic Acids Res* **34**, W63-69 (2006).
51. K. Asanuma, K. N. Campbell, K. Kim, C. Faul, P. Mundel, Nuclear relocation of the nephrin and CD2AP-binding protein dendrin promotes apoptosis of podocytes. *Proceedings of the National Academy of Sciences* **104**, 10134-10139 (2007).
52. F.-X. Theillet *et al.*, Site-specific NMR mapping and time-resolved monitoring of serine and threonine phosphorylation in reconstituted kinase reactions and mammalian cell extracts. *Nature protocols* **8**, 1416 (2013).
53. F.-X. Theillet *et al.*, Structural disorder of monomeric α-synuclein persists in mammalian cells. *Nature* **530**, 45-50 (2016).
54. J. M. Plitzko, B. Schuler, P. Selenko, Structural Biology outside the box-inside the cell. *Curr Opin Struct Biol* **46**, 110-121 (2017).
55. D. Pinotsi *et al.*, Direct Observation of Heterogeneous Amyloid Fibril Growth Kinetics via Two-Color Super-Resolution Microscopy. *Nano Letters* **14**, 339-345 (2014).
56. J. L. Guo *et al.*, Distinct α-synuclein strains differentially promote tau inclusions in neurons. *Cell* **154**, 103-117 (2013).
57. S. Lovestam *et al.*, Seeded assembly in vitro does not replicate the structures of alpha-synuclein filaments from multiple system atrophy. *FEBS Open Bio* **11**, 999-1013 (2021).
58. J. Collinge, Prion strain mutation and selection. *Science* **328**, 1111-1112 (2010).
59. J. Li, S. Browning, S. P. Mahal, A. M. Oelschlegel, C. Weissmann, Darwinian Evolution of Prions in Cell Culture. *Science* **327**, 869-872 (2010).
60. N. Makarava, I. V. Baskakov, The evolution of transmissible prions: the role of deformed templating. *PLoS Pathog* **9**, e1003759 (2013).
61. M. T. Fodero-Tavoletti *et al.*, In Vitro Characterization of Pittsburgh Compound-B Binding to Lewy Bodies. *The Journal of Neuroscience* **27**, 10365-10371 (2007).

62. Y. Kudo *et al.*, 2-(2-[2-Dimethylaminothiazol-5-yl]Ethenyl)-6- (2-[Fluoro]Ethoxy)Benzoxazole: A Novel PET Agent for In Vivo Detection of Dense Amyloid Plaques in Alzheimer's Disease Patients. *Journal of Nuclear Medicine* **48**, 553-561 (2007).
63. L. Kuebler *et al.*, [11C]MODAG-001—towards a PET tracer targeting α-synuclein aggregates. *European Journal of Nuclear Medicine and Molecular Imaging* **48**, 1759-1772 (2021).
64. M. Verdurand *et al.*, In Silico, in Vitro, and in Vivo Evaluation of New Candidates for α-Synuclein PET Imaging. *Molecular Pharmaceutics* **15**, 3153-3166 (2018).
65. M. Verdurand *et al.*, Amyloid-beta radiotracer [18F] BF-227 does not bind to cytoplasmic glial inclusions of postmortem multiple system atrophy brain tissue. *Contrast Media & Molecular Imaging* **2018**, (2018).
66. A. B. Siemer, K.-Y. Huang, A. E. McDermott, Protein linewidth and solvent dynamics in frozen solution NMR. (2012).
67. S. Bahri *et al.*, 1H detection and dynamic nuclear polarization–enhanced NMR of Aβ1-42 fibrils. *Proceedings of the National Academy of Sciences* **119**, e2114413119 (2022).
68. D. Eliezer, E. Kutluay, R. Bussell, Jr., G. Browne, Conformational properties of alpha-synuclein in its free and lipid-associated states. *J Mol Biol* **307**, 1061-1073 (2001).
69. L. Kang *et al.*, N-terminal acetylation of α-synuclein induces increased transient helical propensity and decreased aggregation rates in the intrinsically disordered monomer. *Protein Science* **21**, 911-917 (2012).
70. J. Medeiros *et al.*, Partial magic angle spinning NMR (1)H, (13)C, (15)N resonance assignments of the flexible regions of a monomeric alpha-synuclein: conformation of C-terminus in the lipid-bound and amyloid fibril states. *Biomol NMR Assign* **15**, 297-303 (2021).
71. M. Johnson, A. T. Coulton, M. A. Geeves, D. P. Mulvihill, Targeted amino-terminal acetylation of recombinant proteins in E. coli. *PLoS One* **5**, e15801 (2010).
72. B. Fauvet, H. A. Lashuel, in *Protein Amyloid Aggregation: Methods and Protocols*, D. Eliezer, Ed. (Springer New York, New York, NY, 2016), pp. 3-20.
73. Y. Kim *et al.*, Efficient site-specific labeling of proteins via cysteines. *Bioconjug Chem* **19**, 786-791 (2008).
74. D. N. Mastronarde, Automated electron microscope tomography using robust prediction of specimen movements. *J Struct Biol* **152**, 36-51 (2005).
75. S. H. Scheres, RELION: implementation of a Bayesian approach to cryo-EM structure determination. *J Struct Biol* **180**, 519-530 (2012).
76. R. Fernandez-Leiro, S. H. W. Scheres, A pipeline approach to single-particle processing in RELION. *Acta Crystallogr D Struct Biol* **73**, 496-502 (2017).
77. S. H. W. Scheres, Amyloid structure determination in RELION-3.1. *Acta Crystallogr D Struct Biol* **76**, 94-101 (2020).
78. S. Q. Zheng *et al.*, MotionCor2: anisotropic correction of beam-induced motion for improved cryo-electron microscopy. *Nat Methods* **14**, 331-332 (2017).
79. K. Zhang, Gctf: Real-time CTF determination and correction. *J Struct Biol* **193**, 1-12 (2016).
80. T. Bepler *et al.*, Positive-unlabeled convolutional neural networks for particle picking in cryo-electron micrographs. *Nat Methods* **16**, 1153-1160 (2019).

81. K. Jamali, D. Kimanius, S. H. Scheres, in *The Eleventh International Conference on Learning Representations*. (2022).
82. P. Emsley, B. Lohkamp, W. G. Scott, K. Cowtan, Features and development of Coot. *Acta Crystallogr D Biol Crystallogr* **66**, 486-501 (2010).
83. L. Hunter, T. E. Klein, in *Biocomputing '96*. (WORLD SCIENTIFIC, 1995), pp. 1-774.
84. P. V. Afonine *et al.*, Real-space refinement in PHENIX for cryo-EM and crystallography. *Acta Crystallogr D Struct Biol* **74**, 531-544 (2018).